Supplementary Information

Jiayue Wang[1], Sean R. Bishop[2], Lixin Sun[1], Qiyang Lu[3], Gulin Vardar[1], Roland Bliem[1], Nikolai Tsvetkov[1], Ethan J. Crumlin[4], Jean-Jacques Gallet[5,6], Fabrice Bournel[5,6], Iradwikanari Waluyo[7] & Bilge Yildiz[1,3]

[1]*Department of Nuclear Science and Engineering, Massachusetts Institute of Technology (MIT), Cambridge, USA.*

[2]*Materials Processing Center, MIT, Cambridge, MA, USA.*

[3]*Department of Materials Science and Engineering, MIT, Cambridge, MA, USA.*

[4]*Advanced Light Source, Lawrence Berkeley National Laboratory, Berkeley, CA, USA.*

[5]*Laboratoire de Chimie Physique-Matière et Rayonnement, Sorbonne Universités, Paris, France.*

[6]*Synchrotron SOLEIL, L'Orme des Merisiers, Saint-Aubin, France.*

[7]*National Synchrotron Light Source II, Brookhaven National Laboratory, Upton, NY, USA.*

Supplementary Note 1: Sample characterization

Schematic cross-section of the electrochemical cell is shown in Supplementary Fig. 1a. Ceria films are deposited onto the YSZ (001) substrates which have been pre-decorated with Pt current electrodes. Consequently, the ceria films have two components: the film grown directly on the YSZ substrate and the film grown on Pt grids. A cross-section SEM image is provided to show the uniform coverage of the ceria film over both the YSZ substrates and the Pt grids (Supplementary Fig. 1b).

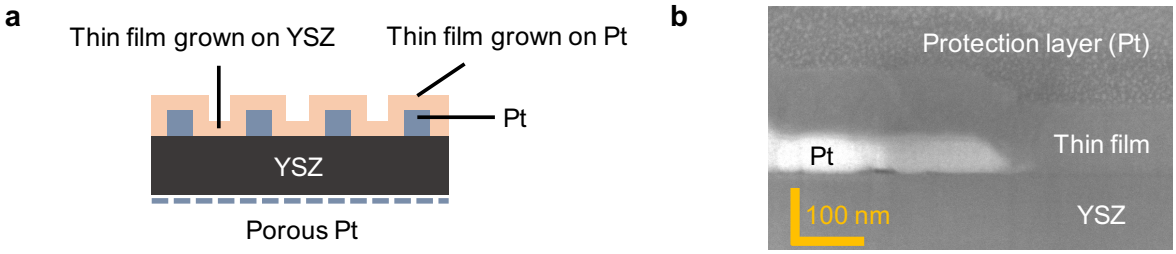

Supplementary Figure 1: Characterization of the electrochemical cell. (a) The schematics of the cross section. (b) SEM image showing a uniform film coverage on YSZ as well as on the Pt grid. The cross section was prepared with focused Ga ion beam. Tilt angle: 53°.

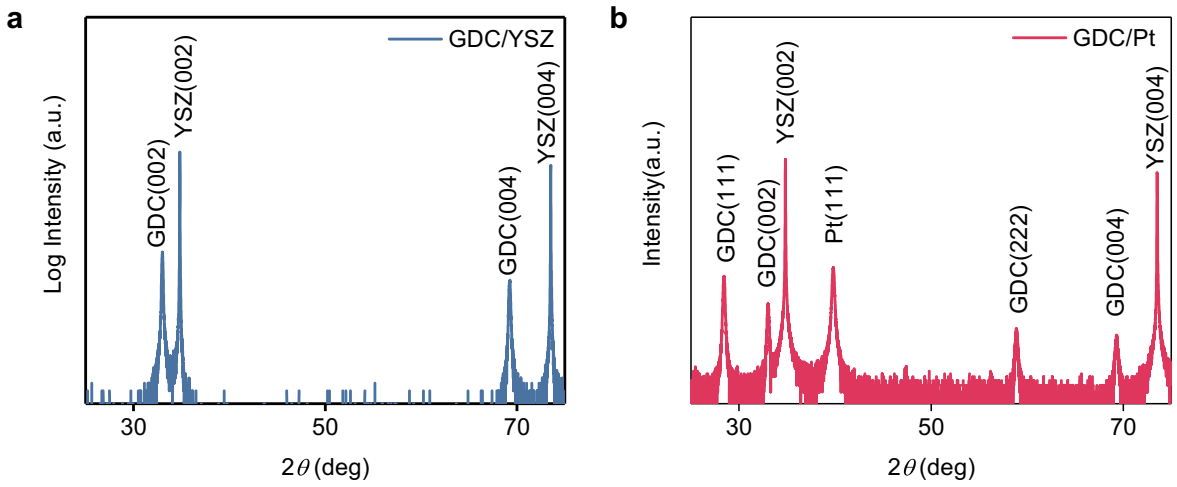

Supplementary Figure 2: High-resolution X-ray diffraction data of symmetric out-of-plane 2θ-ω scan of (a) pristine $Gd_{0.2}Ce_{0.8}O_{1.9}$ (GDC) thin film grown on YSZ (001) substrate without Pt grids, and (b) GDC film directly grown on Pt. While only (001)-type ceria reflection was observed in (a), both (001) and (111) reflections are observed in (b). These results indicate an epitaxial growth of ceria on YSZ (001) substrate, and a mixed (001) and (111) growth texture on Pt grids.

To better demonstrate the film quality, a two-dimensional XRD was collected on $Gd_{0.5}Ce_{0.5}O_{1.75}$ with a Bruker D8 Discover X-ray diffractometer equipped with GADDS. Supplementary Fig. 3a shows the 2D diffraction pattern near the fluorite (113) reflection at grazing incidence, where the bright (113) reflection spot indicates a highly textured films. Some (113) reflection along the chi direction is also observed, which indicates the ceria films grown on Pt is not epitaxial. However, the intensity for this non-epitaxial reflection is much weaker than the epitaxial (113) reflection.

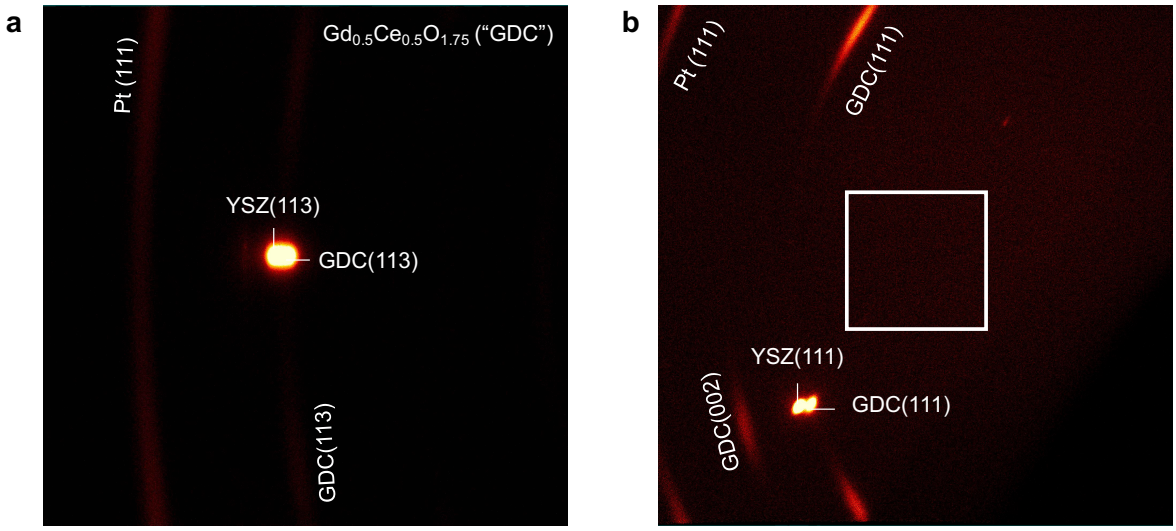

Supplementary Figure 3: 2D X-ray diffraction on the $Gd_{0.5}Ce_{0.5}O_{1.75}$ electrochemical cell after carbon deposition test. (a) The symmetric scan collected at grazing incidence near the fluorite (113) reflection shows the polycrystalline Pt grids and highly textured ceria thin film. (b) Verification of the fluorite structure of $Gd_{0.5}Ce_{0.5}O_{1.75}$ thin films. No reflection was observed near the Ia-3 (112) reflection peak (denoted by the white border box) in the skew-symmetric scan. Therefore, we conclude the $Gd_{0.5}Ce_{0.5}O_{1.75}$ thin films to be in fluorite structure.

$Gd_{0.5}Ce_{0.5}O_{1.75}$ structures have been reported as either fluorite phase[1] (space group $\mathrm{Fm\bar{3}m}$) or cubic phase[2] (space group Ia-3). Since the lattice parameter of the cubic phase is about two times that of the fluorite phase, the peaks common to these two structures appear to be superimposed[3]. The only difference is the cubic phase would have some additional peaks due to symmetry breaking from the disordered Gd/Ce and O sites. Among all these additional peaks, the strongest one is Ia-3 (112). Therefore, we collected a 2D skew-symmetric scan near the Ia-3 (112) reflection pattern and the result is shown in Supplementary Fig. 3b. The 2D reflection pattern were collected when the sample was rotating from $\varphi = 0°$ to $\varphi = 360°$, in other words, Supplementary Fig. 3b shows a φ-averaged skew-symmetric scan. No (112) reflection from the Ia-3 phase was observed, we

therefore conclude the $Gd_{0.5}Ce_{0.5}O_{1.75}$ films to be fluorite phase.

Similarly, $Zr_{0.5}Ce_{0.5}O_2$ could also have either a tetragonal[4] (space group $P4_{2/nmc}$) or a cubic structure[5] (space group $Fm\bar{3}m$), depending on the preparation method. Since the out-of-plane lattice parameter of the cubic and tetragonal phase are similar, we collected the in-plane XRD data on a $Zr_{0.5}Ce_{0.5}O_2$ film without Pt grid (to prevent X-ray attenuation in the Pt). The in-plane symmetric scan was collected at grazing incidence (1 degree) on a Rigaku SmartLab X-ray diffractometer using Cu K-alpha 1 radiation and the result is shown in Supplementary Fig. 4. Since only the fluorite diffraction patterns are observed, we conclude the $Zr_{0.5}Ce_{0.5}O_2$ film to be fluorite cubic phase.

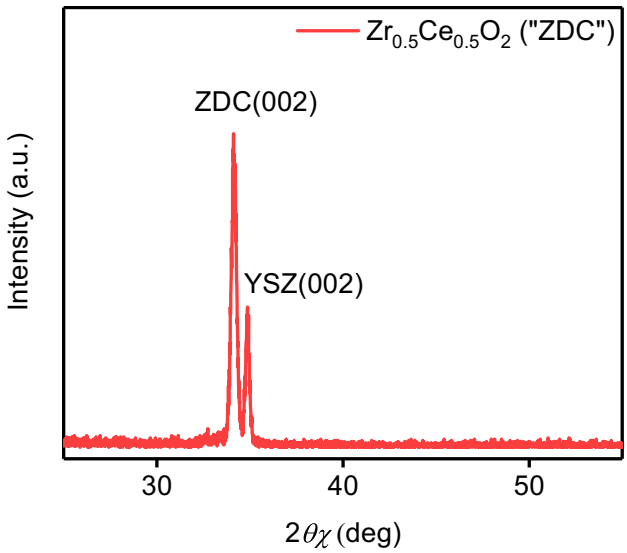

Supplementary Figure 4: Verification of the fluorite structure of $Zr_{0.5}Ce_{0.5}O_2$ thin films. X-ray diffraction data of symmetric in-plane scan of the pristine $Zr_{0.5}Ce_{0.5}O_2$ thin film without Pt grids. Only fluorite ZDC reflection was observed. Therefore, we conclude the $Zr_{0.5}Ce_{0.5}O_2$ thin films to be in fluorite structure.

To assess the surface morphological change during carbon deposition, scanning electron microscope (SEM) images were collected on the CeO_2 working electrodes (with 10 nm carbon

coating) before and after experiments. As shown in Supplementary Fig. 5a, no cracks were observed on the thin film. In addition, a Veeco Metrology Nanoscope IV-Dimension 3100 atomic force microscope (AFM) operated in Tapping Mode was used to characterize the surface morphology (Supplementary Fig. 5b). The thin films grown on the YSZ substrate demonstrated compacted grains of similar size, whereas the ones on the Pt grids showed larger and scattered grain sizes. Nevertheless, no significant morphological differences were observed before and after the experiment, indicating the possible morphology change would have no impact on the carbon deposition behavior.

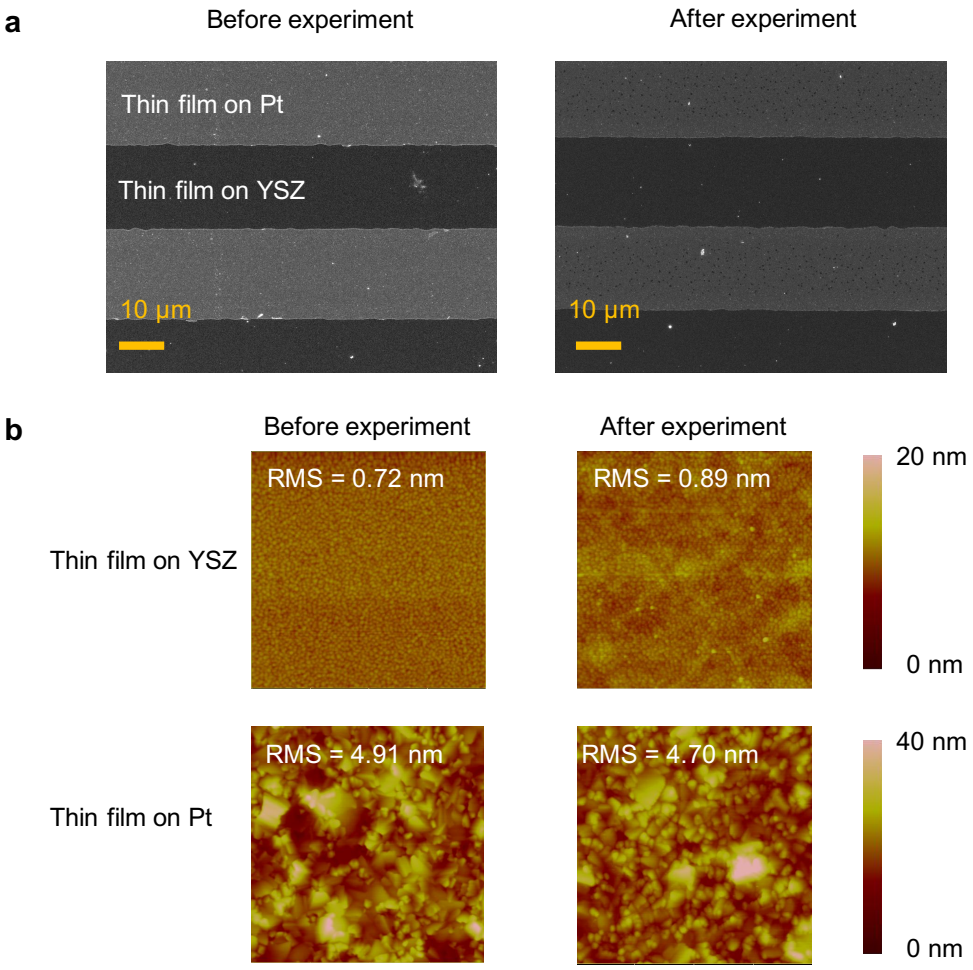

Supplementary Figure 5: (a) SEM and (b) AFM image of the thin-film CeO_2 working electrodes before and after experiment. No significant morphological change was observed. SEM images were collected on ceria films with 10 nm carbon coating. Field of view for the AFM images: 1 μm.

Supplementary Note 2: XPS peak assignment: CO, CO_2 gas phase

A typical C 1*s* spectra during carbon deposition on ceria-based thin film is shown in Supplementary Fig. 6a. To better understand the two features at around 292 eV (shaded region), we compare the C 1*s* spectra collected on the sample and the C 1*s* spectra collected with sample extracted (Supplementary Fig. 6b). Since we are only probing the gas atmosphere, the two distinct features in Supplementary Fig. 6b arise from CO and CO_2 gas phase [6,7], respectively. For Supplementary Fig. 6b, we calibrate the binding energy by aligning the CO_2 gas peak at 293.5 eV[8]. As the binding energy in Supplementary Fig. 6a were calibrated by aligning the Ce $4d_{3/2}$ peak at 122 eV[9], we cannot directly compare the binding energy in Supplementary Fig. 6a and 6b. Nonetheless, as the peak separations in Supplementary Fig. 6a and 6b are rather similar ($\sim$1.5 eV), we conclude the features at around 292 eV in the C 1*s* spectra to be CO and CO_2 gas phase.

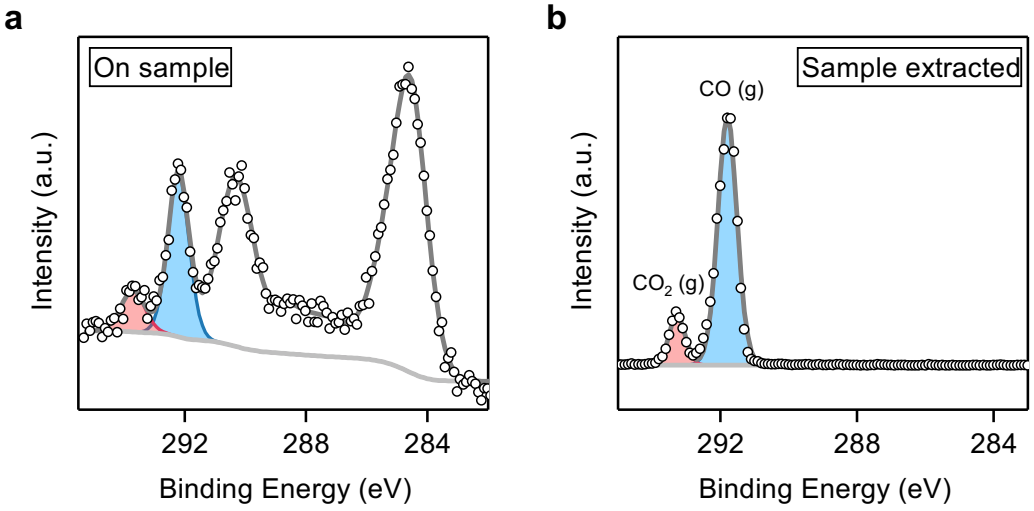

Supplementary Figure 6: C 1*s* spectra collected (a) on $Zr_{0.5}Ce_{0.5}O_2$ and (b) with sample extracted. Data were collected in 0.3 Torr 9 : 1 CO/CO_2 atmosphere at 450 °C.

Supplementary Note 3: Evolution of surface chemistry

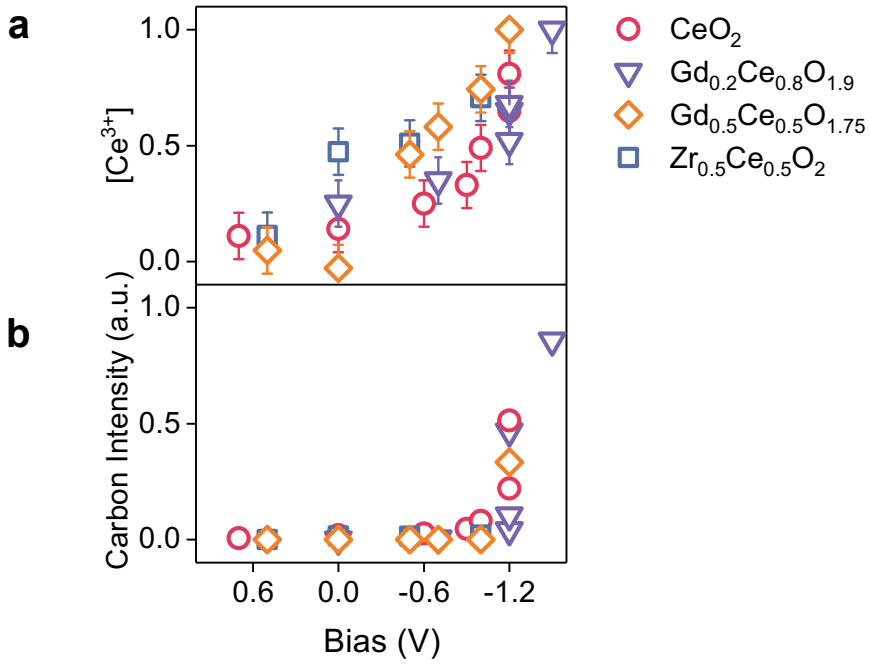

Supplementary Figure 7: Evolution of surface chemistry during carbon deposition. (a) Surface reduction state ($[Ce^{3+}]$) and (b) carbon deposition at 450 °C in 0.3 Torr 9 : 1 CO/CO_2 as a function of applied electrical bias.

Supplementary Note 4: Quantification of carbon intensity

Since signals from surface elements such as Ce may get attenuated during carbon deposition, the total area of CO gas peak was selected as the normalization factor for carbon quantification. To validate our choice, Supplementary Fig. 8 shows the XPS intensities of the deposited carbon, Ce 4*d*, and CO gas peak on $Gd_{0.2}Ce_{0.8}O_{1.9}$ during the measurement. As can be seen, the CO gas peak remained rather stable throughout the polarization experiment whereas the Ce 4d peak lost almost half of its intensity after carbon deposition.

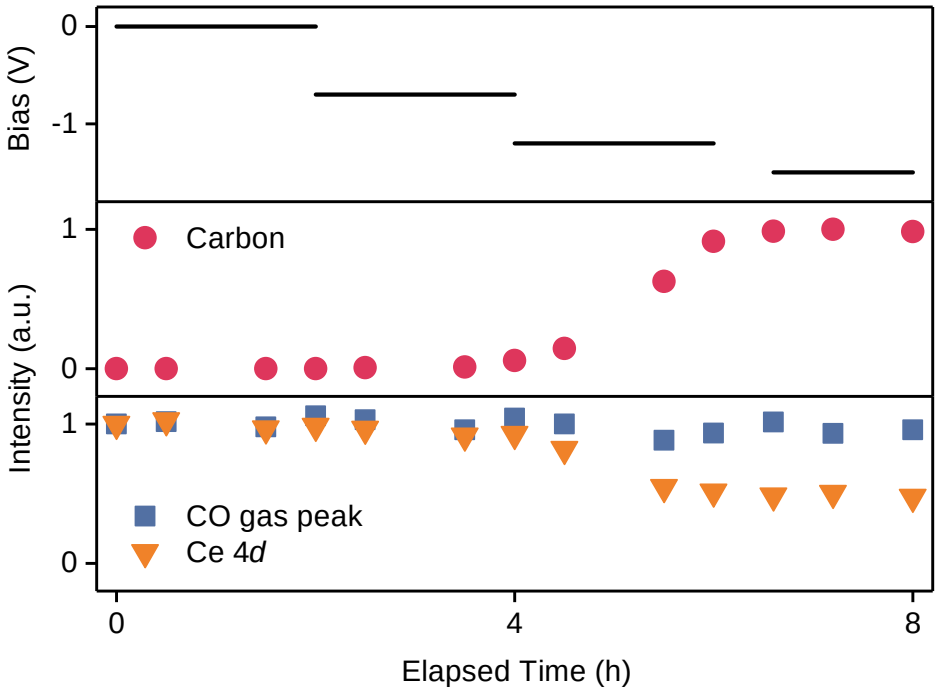

Supplementary Figure 8: Normalization method: the corresponding CO gas peak. Time-dependent study showing CO gas peak remained rather stable throughout the polarization experiment while the intensity of Ce 4*d* peak decreased after carbon deposition. Data collected on $Gd_{0.2}Ce_{0.8}O_{1.9}$ in 0.3 Torr $9:1$ CO/CO_2 atmosphere at 450 °C. To ease comparison, the intensities of CO and Ce 4*d* peaks shown in the plot are normalized to their initial value (i.e., the first data point).

For $u = xy$, the standard deviation can be calculated from [10]:

$$\frac{\Delta u}{u} = \sqrt{\left(\frac{\Delta x}{x}\right)^2 + \left(\frac{\Delta y}{y}\right)^2} \tag{1}$$

Since carbon quantity is normalized to the CO gas peak, the error bar for the normalized

deposited carbon quantity $X = I(\mathrm{carbon})/I(\mathrm{CO})$ can be calculated as:

$$\frac{\Delta X}{X} = \sqrt{\left(\frac{\Delta I(\mathrm{carbon})}{I(\mathrm{carbon})}\right)^2 + \left(\frac{\Delta I(\mathrm{CO})}{I(\mathrm{CO})}\right)^2}, \tag{2}$$

where the uncertainty for individual peak intensity is obtained from CasaXPS software.

Supplementary Note 5: Quantification of [Ce^{3+}]

The concentration of surface Ce^{3+} sites has been calculated from Ce $4d$ peak. The two highest binding energy components were assigned to Ce^{4+} species [11]. These two peaks refer to Ce $4d_{5/2}$ and Ce $4d_{3/2}$, with a spin-orbit splitting of 3.3 eV [9,12]. The area of this doublet is calculated through peak fitting, denoted with $I(\mathrm{Ce}^{4+})$. The fitting constraints were set so that the two fitted peaks are separated by 3.3 eV, and the area ratio is fixed at $2:3$, as shown in Supplementary Fig. 9a.

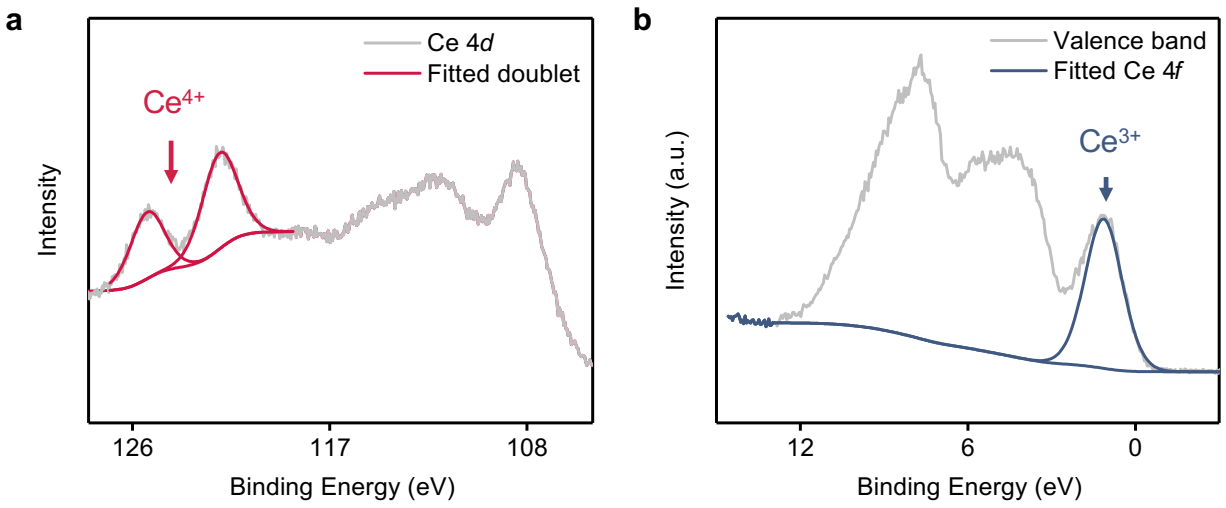

Supplementary Figure 9: [Ce^{3+}] quantification from (a) Ce $4d$ and (b) Ce $4f$ spectra. The doublet in Ce $4d$ spectra is fitted with a fixed separation of 3.3 eV and area ratio of $2:3$. Peaks were fitted with a 30% Lorentz/Gaussian line shape over a Shirley background.

Since surface Ce^{4+} concentration is directly related to the intensity of the doublet, [Ce^{3+}] can be quantified as [13]:

$$[\mathrm{Ce^{3+}}] = 1 - [\mathrm{Ce^{4+}}] = 1 - \frac{I(\mathrm{Ce}\ 4d)_{ref}}{I(\mathrm{Ce}\ 4d)} \frac{I(\mathrm{Ce^{4+}})}{I(\mathrm{Ce^{4+}})_{\mathrm{ref}}}, \tag{3}$$

with "ref" represents the fully oxidized condition ([Ce^{3+}] = 0). The fully oxidized spectra were collected at the beginning of each experiment in 20 mTorr O_2 at 350 °C, where a complete absence of the Ce $4f$ peak in the valence band was considered as the sign of a full oxidation.

As shown in previous study, Ce $4f$ peak is only attributed from Ce^{3+} species, and the normalized Ce $4f$ peak intensity ($I(\mathrm{Ce}\ 4f)/(\mathrm{Ce}\ 4d)$) is proportional to surface Ce^{3+} concentration [13–15].

Therefore, as a sanity check, all the calculated [Ce^{3+}] values used in this paper are compared with the corresponding normalized Ce $4f$ intensities. The relation between [Ce^{3+}] and normalized Ce $4f$ intensity is shown in Supplementary Fig. 10. As can be seen from the linear relationship, the overall agreement between the quantified [Ce^{3+}] and the normalized Ce $4f$ intensity is satisfactory. In this work, we took the maximum deviation between the quantified [Ce^{3+}] and linear fitting as the error bar.

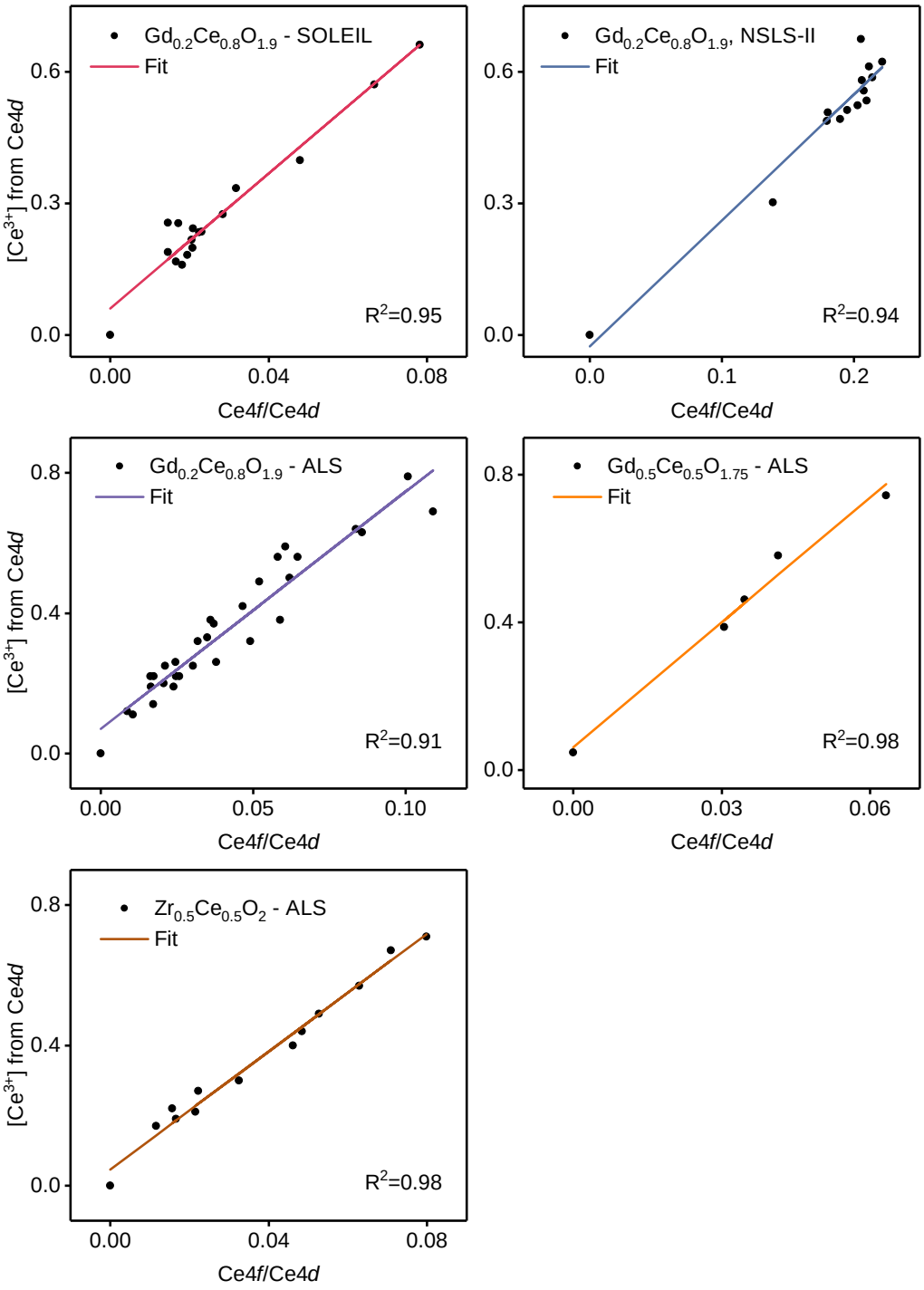

Supplementary Figure 10: Validation for [Ce^{3+}] quantification for each sample studied in this work. The Ce^{3+} concentrations obtained from Ce $4d$ peaks demonstrate a good linear correlation with normalized Ce $4f$ peak intensity. The error bar was then estimated from the maximum deviation, which is 10%. The legends such as "SOLEIL", "ALS", and "NSLS-II" indicate at which beamline the data were collected.

Supplementary Note 6: Quantification of surface dopant concentration from XPS

For homogeneous materials, the total emitted electron intensity from an individual element can be expressed as [16]

$$I \propto \sigma \cdot c \cdot \lambda(E) \cdot G(E) \cdot \phi \cdot D, \tag{4}$$

where $\sigma, c, \lambda, G, E, \phi, D$ represent photoionization cross section, atomic concentration, attenuation depth, analyzer efficiency, electron kinetic energy, photon flux and geometrical factor (e.g., electron emission angle), respectively. In addition, $\lambda(E)$ and $G(E)$ follow approximately [16]

$$\begin{aligned} G(E) &\propto \frac{1}{E} \\ \lambda(E) &\propto E^{0.75} \end{aligned} \tag{5}$$

For cations A and B in a material that are measured in one single experiment, ϕ and D cancel out. Therefore, the concentration ratio of these two cations can be calculated as:

$$\begin{aligned} \frac{c_{\mathrm{A}}}{c_{\mathrm{B}}} &= \frac{I_{\mathrm{A}}}{I_{\mathrm{B}}} \frac{\sigma_{\mathrm{B}} \lambda_{\mathrm{B}} G_{\mathrm{B}}}{\sigma_{\mathrm{A}} \lambda_{\mathrm{A}} G_{\mathrm{A}}} \\ &= \frac{I_{\mathrm{A}}}{I_{\mathrm{B}}} \frac{\sigma_{\mathrm{B}}}{\sigma_{\mathrm{A}}} \left(\frac{E_{\mathrm{A}}}{E_{\mathrm{B}}} \right)^{0.25} \end{aligned} \tag{6}$$

Surface dopant concentrations were calculated as cation fraction, i.e., dopant/(dopant+Ce). Peaks used for analysis were Ce $4d$, Zr $3d$, and Gd $4d$, respectively. The photoionization cross

sections were adopted from Ref. 17, as shown in Table 1.

The error in quantifying the surface composition may arise from two parts: first of all, the random error Δ_{rand} that exists during the APXPS measurement (e.g., variation of photon flux and local atmosphere) and data analysis (e.g., background subtraction); secondly, the systematic error Δ_{sys} in data analysis (e.g., the accuracy of the photoionization cross section).

To address the random error Δ_{rand}, surface composition were calculated on $Gd_{0.2}Ce_{0.8}O_{1.9}$ sample in 0.15 Torr $9:1$ CO/CO_2 mixture under a constant -0.5 V cathodic bias as a function of time. As shown in Supplementary Fig. 11, surface Gd concentration has around 1% fluctuation during the 5-hour measurement. Since the surface chemistry remained stable during the measurement (Fig. 3), the observed 1% fluctuation reflects the random error Δ_{rand}.

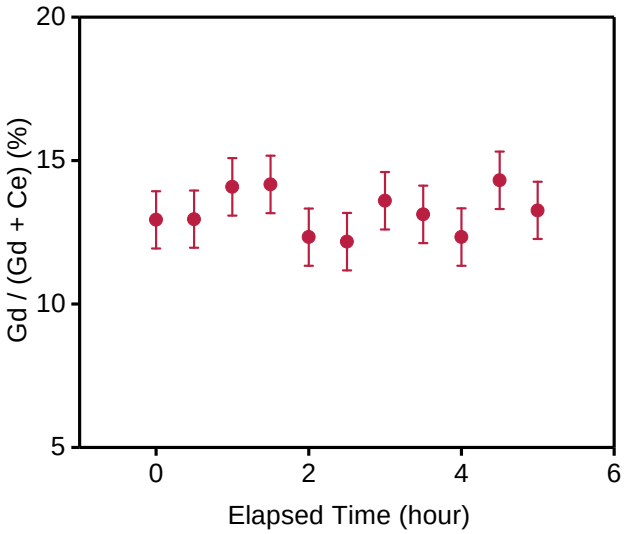

Supplementary Figure 11: Time-dependent surface Gd concentration of $Gd_{0.2}Ce_{0.8}O_{1.9}$ upon exposure to 0.15 Torr 9:1 CO/CO_2 mixture at 450 °C. The 1% standard deviation was adopted as Δ_{rand} in this paper .

Table 1: Photoionization cross sections at 400 eV (Mb)

Ce 4d	Zr 3d	Gd 4d
0.9	3.0	0.8

Secondly, to address the systematic error Δ_{sys}, we compare the surface composition quantified from both lab-based XPS spectra (UHV, room temperature) and the APXPS spectra (20 mTorr O_2, 350 °C). For the spectra collected with lab-based XPS, data analysis was done by using the Multipak software package, a proprietary data processing software of Physical Electronics (PHI). The comparison is summarized in Fig. 2c and we assign the variation of the calculated dopant concentration from the two methods as the systematic error Δ_{sys}.

As a result, the error bar of surface composition quantification Δ was calculated as:

$$\Delta = \sqrt{\Delta_{\mathrm{rand}}^2 + \Delta_{\mathrm{sys}}^2} \tag{7}$$

Supplementary Note 7: Preferential carbon deposition

As shown in Fig. 2c, after the threshold carbon deposition, an apparent increase was observed for the Gd/(Gd + Ce) ratio on $Gd_{0.2}Ce_{0.8}O_{1.9}$ and $Gd_{0.5}Ce_{0.5}O_{1.75}$. This originates from the fact that more carbon was deposited onto the Ce site rather than onto the Gd site.

To better demonstrate this phenomenon, Supplementary Fig. 12 shows the Gd 4*d* and Ce 4*d* spectra on $Gd_{0.5}Ce_{0.5}O_{1.75}$, collected before and after the threshold carbon deposition at the same condition (i.e., same temperature, atmosphere, and electrical polarization). For the Ce 4*d* spectra, the new broad feature above 120 eV is from the carbon KVV Auger peak[18]. Besides the Auger feature, it can be clearly seen that the intensity of Ce 4*d* decreased after the carbon deposition. The

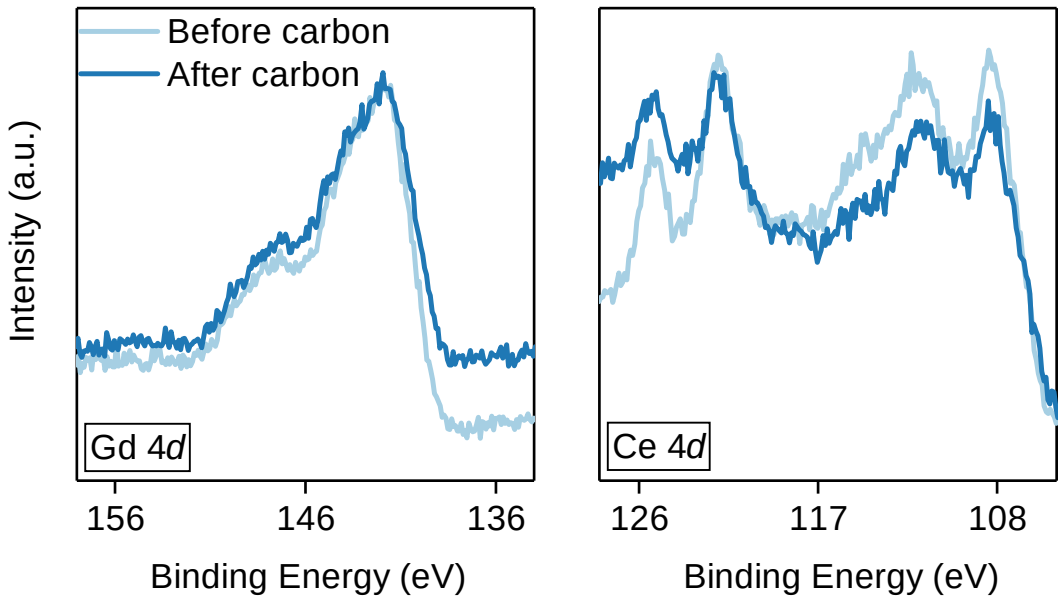

Supplementary Figure 12: Gd 4*d* and Ce 4*d* spectra of $Gd_{0.5}Ce_{0.5}O_{1.75}$ before and after the threshold carbon deposition. Data were collected at 450 °C in 0.3 Torr 9 : 1 CO/CO_2, under +0.5 V anodic bias. After carbon deposition, the intensity of Ce 4*d* decreased while the Gd 4*d* spectra remained almost the same. This phenomenon clearly indicates that carbon are more favorable deposited onto the Ce sites rather than the Gd sites.

decreased Ce 4*d* intensity is due to the signal attenuation from the deposited carbon. On the other hand, the intensity of Gd 4*d* remained almost the same before and after carbon deposition whereas the increased background level near 136 eV is from the carbon KVV Auger peak.

The observed spectra intensity change clearly demonstrates that the Ce 4*d* intensity got more attenuated during the carbon deposition, indicating carbon atoms are preferentially to be deposited onto the Ce sites rather than the Gd sites.

Supplementary Note 8: Carbon saturation and removal

Following the time-dependent experiment shown in Fig. 3, we further increased the cathodic bias to -1.5 V but found the carbon peak did not increase. This carbon growth saturation can be clearly visualized by the time-dependent C 1*s* spectra shown in Supplementary Fig. 13. As shown in the plot, both C 1*s* spectra collected at 400 eV and 650 eV remained stable during the 1.5-hour measurement, indicating the carbon stopped growing on the surface.

As the total intensity of Ce 4*d* halved after the carbon deposition (Supplementary Fig. 8), we can roughly estimate the saturated carbon thickness to be around 4.2 Å (1-2 monolayers of graphite) and the calculation is as follows:

Consider a simple model where the ceria surface is covered by a uniform and smooth graphitic layer with thickness *d*. The attenuation of the signal strength of Ce 4*d* (I) by the graphitic layer can be expressed as[16]:

$$I = I^0 \times \exp\left(-\frac{d}{\lambda \cos\theta}\right), \tag{8}$$

where I^0, λ, and θ denote the signal intensity from the ceria thin film without carbon, attenuation length of the electron, and the take-off angle (the off-axis angle with respect to the surface normal[19]).

The inelastic mean free path (IMFP) of an electron with 270 eV kinetic energy (i,e, the Ce

4d spectra at 400 eV photon energy) in graphitic carbon is around 7.1 Å[20]. Since the attenuation length is typically 15-20% smaller than the IMFP[16], here we assign $\lambda = 6$ Å. In addition, as the sample is normal to the detector (ALS, beamline 9.3.2) during measurement, $\theta = 0$. Consequently, we can roughly estimate the film thickness d to be

$$d = -\ln\left(\frac{I}{I^0}\right) \times \lambda \cos\theta = 4.2 \text{ Å}, \tag{9}$$

which corresponds to the thickness of 1-2 monolayers of graphite.

This self-limited carbon growth has also been observed in the previous study, showing the graphene growth on Cu terminates once the surface is fully covered.[21]

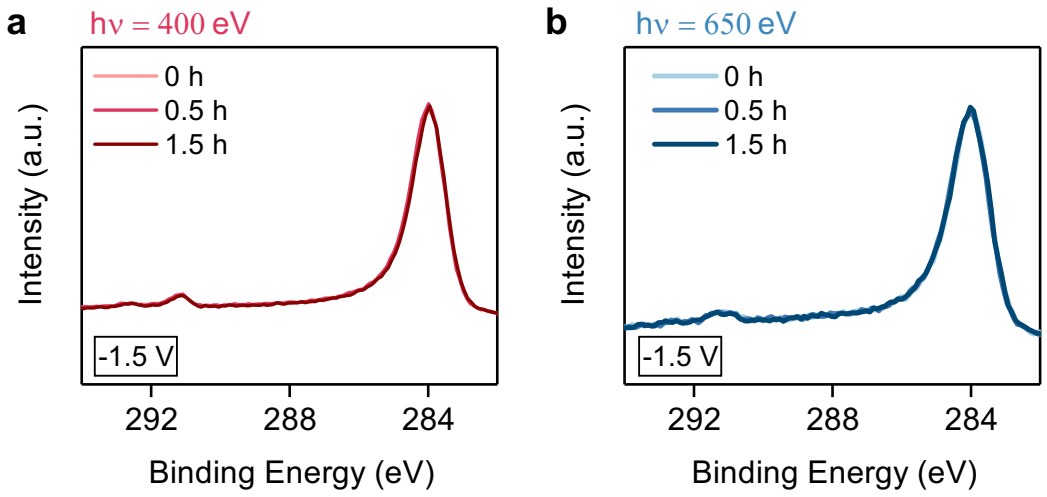

Supplementary Figure 13: Time-dependent C 1s spectra collected under 1.5 V cathodic polarization at a photon energy of (a) 400 eV and (b) 650 eV. Both spectra remained stable during the 1.5-hour measurement, indicating a carbon growth saturation.

In addition, it was observed that the surface carbon after the threshold deposition can be very difficult to remove. As shown in Supplementary Fig. 14a, the surface carbon on $Zr_{0.5}Ce_{0.5}O_2$ before the threshold deposition can be easily removed from anodic polarization. In contrast to this, for $Gd_{0.2}Ce_{0.8}O_{1.9}$ after the threshold carbon deposition, the surface carbon did not decrease even after 0.5 hours of anodic polarization (Supplementary Fig. 14b).

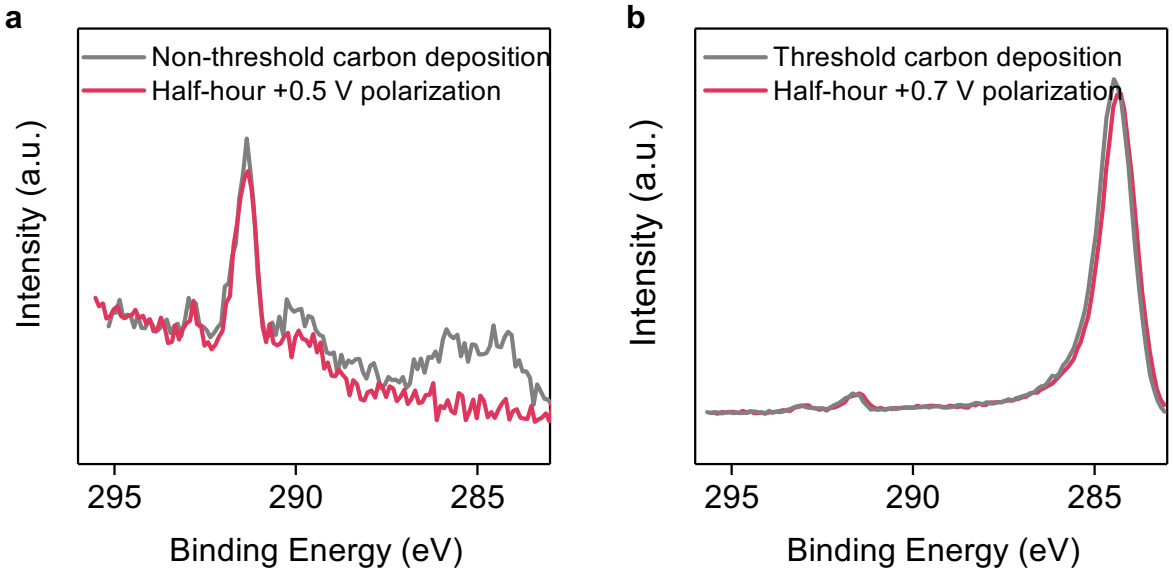

Supplementary Figure 14: Carbon removal (a) before and (b) after the threshold carbon deposition. (a) Carbon can be easily removed on $Zr_{0.5}Ce_{0.5}O_2$ with 0.5 V anodic bias. (b) Carbon intensity did not decrease on $Gd_{0.2}Ce_{0.8}O_{1.9}$ even with 0.7 V anodic polarization. Both spectra were collected at 450 °C in 0.3 Torr 9:1 CO/CO_2 atmosphere.

Supplementary Note 9: Surface overpotential

According to the Nernst equation, application of an overpotential (η) could change the chemical potential of oxygen ($\Delta\mu_O$) within the working electrode[22,23]:

$$\Delta\mu_O = 4F\eta, \tag{10}$$

where *F* denotes the Faraday constant.

Previous studies have demonstrated that when the electronic defects are the minority defect species in the materials, a change in $\Delta\mu_O$ changes the chemical potential of electrons ($\Delta\mu_e$)[22]:

$$\Delta\mu_e = -\frac{1}{4}\Delta\mu_O = -F\eta \tag{11}$$

Consequently, the Fermi level (E_F) would change with overpotential as[22]:

$$E_F = \frac{\Delta\mu_e}{F} = -\eta \tag{12}$$

Under these circumstances, the binding energy (E_B) shifts of non-redox-active elements,

measured with XPS, can be used to quantify the surface overpotential[24]

$$\eta = -\frac{\Delta E_B}{e} \tag{13}$$

where e = 1 eV/V. As an example, this -1 eV/V relation has been observed between the binding energy shift and overpotential on Sm-doped ceria[13] as well as on $La_{0.6}Sr_{0.4}FeO_3$[22] in reducing environment.

Inspired by this, we quantified binding energy shift of Si 2*p* (Supplementary Fig. 15) as Si is a common inert element in all the ceria-based films. The Si peak shift as a function of applied bias is shown in Supplementary Fig. 16. In addition, the binding energy shift of Zr 3*d* in $Zr_{0.5}Ce_{0.5}O_2$ is also shown as a reference. As can be seen, the peak shifts quantified by both peaks match quite well, validating our choice of using Si peak to quantify the binding energy shift.

Feng *et al.* have observed a -1eV/V relation between the binding energy shift and the surface overpotential on 20% Sm-dopoed ceria[13]. As the Brouwer diagrams of Gd-doped and Sm-doped ceria are very similar[25], we would expect the surface overpotential of $Gd_{0.2}Ce_{0.8}O_{1.9}$ and $Gd_{0.5}Ce_{0.5}O_{1.75}$ can be also quantified with Eq. 13. Therefore, we can plot the carbon deposition as a function of overpotential for $Gd_{0.2}Ce_{0.8}O_{1.9}$ and $Gd_{0.5}Ce_{0.5}O_{1.75}$, and the result is shown in Supplementary Fig. 17.

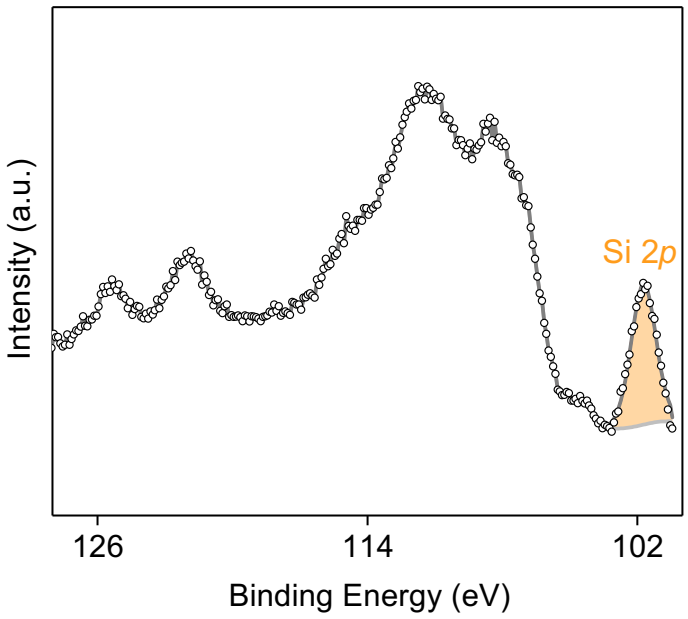

Supplementary Figure 15: An example of Si 2*p* peak used to quantify the peak shift.

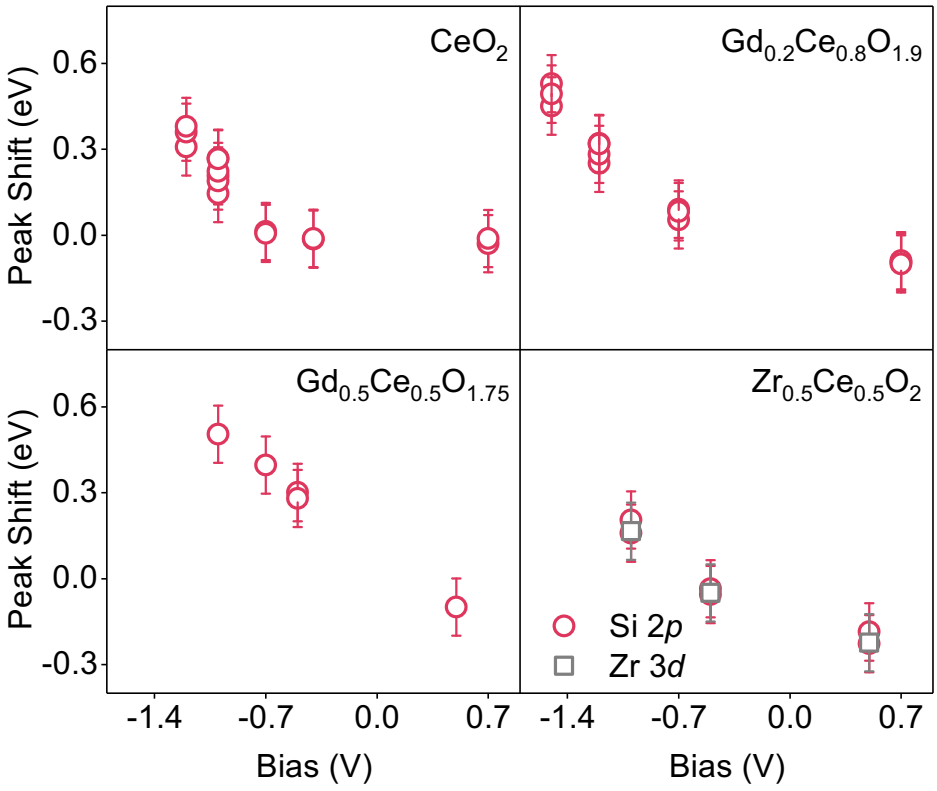

Supplementary Figure 16: Binding energy shift as a function of applied bias on four types of ceria-based thin films at 450 °C in 0.3 Torr 9:1 CO/CO_2. The binding energy shift was quantified from Si 2*p* and Zr 3*d* spectra, respectively.

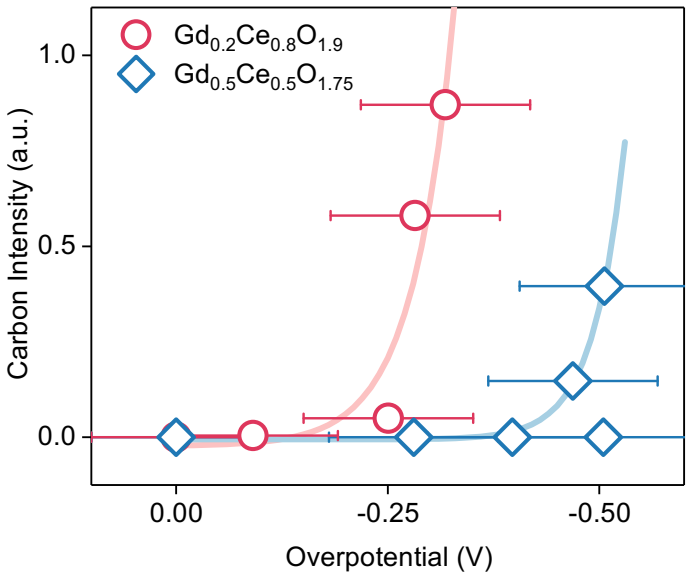

Supplementary Figure 17: Carbon deposition on Gd-doped ceia at different overpotentials in 9:1 CO/CO_2 environment. Note carbon deposition starts at different overpotentials for $Gd_{0.2}Ce_{0.8}O_{1.9}$ and $Gd_{0.5}Ce_{0.5}O_{1.75}$, indicating the surface overpotential cannot explain the threshold carbon onset. The lines are the guide for the eye.

Supplementary Note 10: Carbon-induced Ce^{3+} enrichment

As shown in the time-dependent study in Fig. 3, along with the threshold carbon deposition, the surface Ce^{4+} species vanished. We first verify the observed increase of Ce^{3+} concentration does not originate from a misinterpretation of the XPS data.

After carbon deposition, signals from the ceria thin films got attenuated. Consequently, the deposited carbon layer would decrease the probing depth in the ceria film, making the XPS spectra more "surface sensitive". In other words, the Ce 4*d* spectra collected after the threshold carbon deposition would contain more chemical information from the very surface Ce compared to those collected before carbon deposition. As surface Ce can be more reduced than the sub-surface[14],

the measured [Ce^{3+}] may consequently increase after carbon deposition. In this scenario, it is *possible* that the measured [Ce^{3+}] increase while surface chemistry remains the same. To exclude this possibility, Ce 4*d* spectra were collected at photon energies of both 400 and 650 eV on CeO_2. As shown in Supplementary Fig. 18, even Ce 4*d* spectra collected at 400 eV are more surface sensitive than the ones from 650 eV, the calculated [Ce^{3+}] from both photon energies did not exhibit significant differences. In particular, [Ce^{3+}] quantified from both photon energies exhibited a similar carbon-induced [Ce^{3+}] enrichment (the two data sets at -1.2 V bias). Therefore, the surface did become more Ce^{3+}-enriched during the threshold carbon deposition.

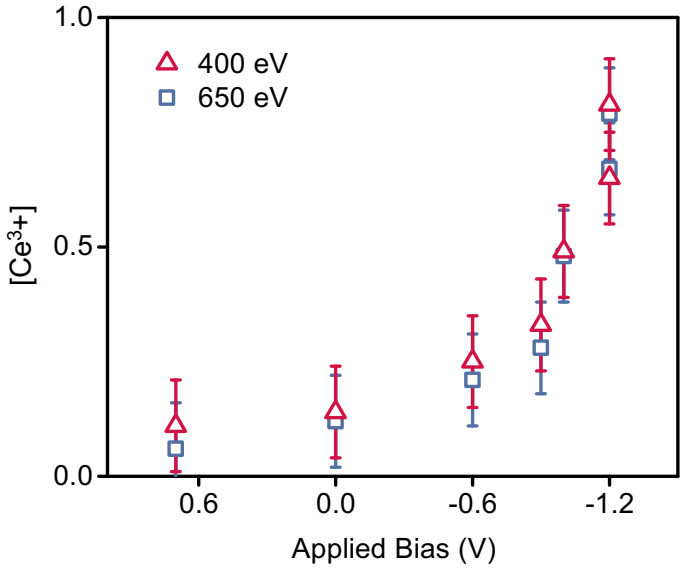

Supplementary Figure 18: [Ce^{3+}] quantified from Ce 4*d* spectra collected at 400 eV and 650 eV on CeO_2. No considerable difference was observed between the quantification from two photon energies. Data collected at 450 °C in 0.3 Torr 9:1 CO/CO_2 atmosphere.

Here we briefly discuss two possible origins of this carbon-induced Ce^{3+} enrichment. First of all, this could originate from the electrochemical polarization. According to the Nernst equation, a cathodic polarization would result in a more reduced surface[23], which have also been observed

in our experiment (Fig. 2). Since the ceria working electrode is not the only source of resistance in our cell (electrolyte, counter electrode, and wiring are the others), only part of the applied voltage drops as an overpotential at the working electrode (Supplementary Fig. 19). After carbon deposition, the surface resistance could increase as carbon can block the active sites. An increase of the surface resistance of the ceria working electrode consequently increases the voltage drop (i.e. the overpotential) at the working electrode thus causing a stronger degree of reduction, which becomes visible in XPS as a higher Ce^{3+} fraction. Secondly, the observed [Ce^{3+}] increase can be also due to the deposited carbon atoms. In this case, it can either be a surface oxygen removal from carbon combustion[26] or a charge transfer[27] from the deposited carbon to the surface Ce atom (cation reduction without oxygen removal). Further studies are suggested to unravel this intriguing phenomenon.

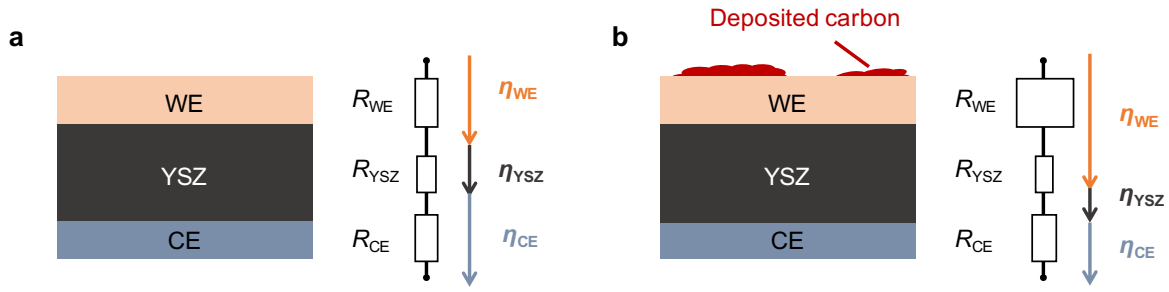

Supplementary Figure 19: Schematics of the relation between surface overpotential and applied bias (a) before and (b) after carbon deposition. After carbon deposition, the surface resistance (R_{WE}) could increase, resulting in an increase in surface overpotential (η_{WE}). WE and CE denote the working electrode and counter electrode, respectively.

Supplementary Note 11: Monte carlo simulation

At each [Ce^{3+}] and doping ratio, 100 random initial configurations were generated. For each initial configuration, 500 Monte Carlo steps (MCS) were employed to ensure equilibrium (Supplementary Fig. 20a), and the averaged value from 300 to 500 MCS were interpreted as the Ce^{3+}-Ce^{3+} pair number formed on this configurations. Finally, the Ce^{3+}-Ce^{3+} pair number formed at each [Ce^{3+}] were obtained by averaging over 100 random initial configurations, as shown in Supplementary Fig. 20b. The error bar was estimated from the standard deviation (STD) over 100 initial configurations. The Ce pair calculation principle is illustrated in Supplementary Fig. 21.

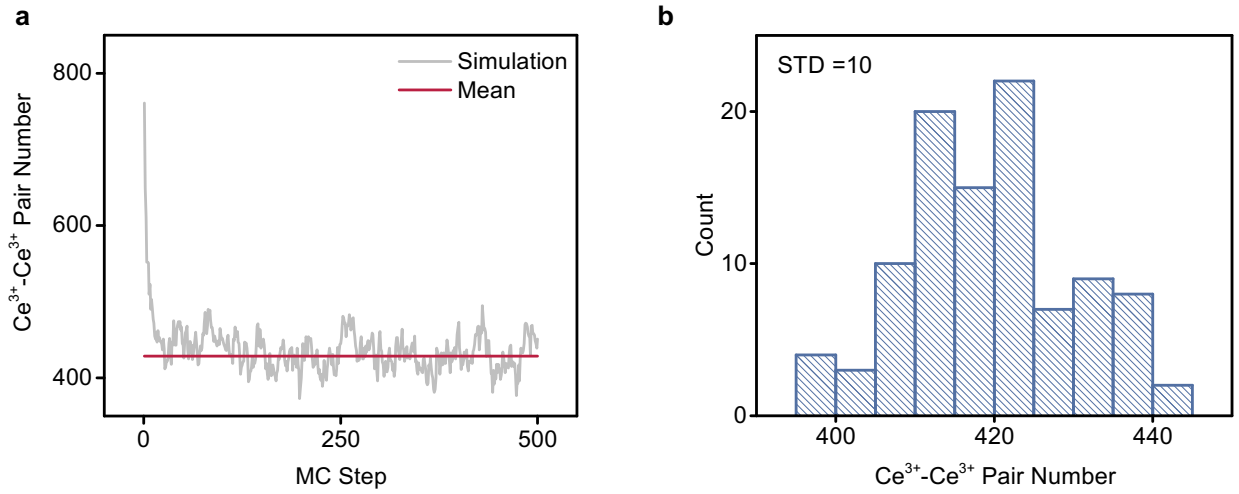

Supplementary Figure 20: Validation for Monte Carlo simulation. (a) Sensitivity of simulation result to Monte Carlo step (MCS). The horizontal line represents the averaged value between MCS 300 to 500. (b) Sensitivity of simulation result to initial lattice configurations. Histogram of the calculated Ce^{3+}-Ce^{3+} pair from 100 different random initial configurations. Data calculated at 50% [Ce^{3+}] with 10% dopant.

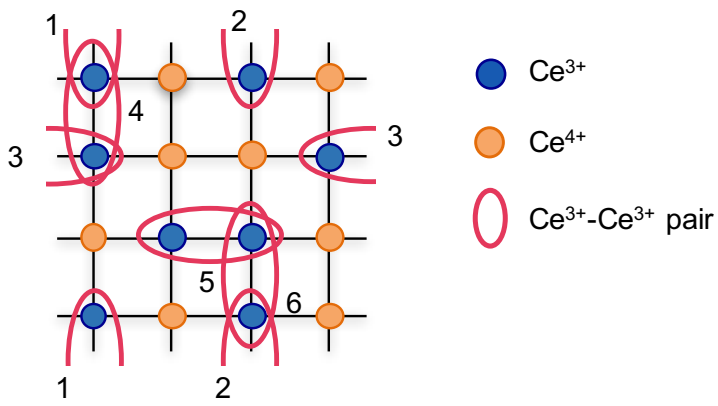

Supplementary Figure 21: Ce pair calculation. In this work, a periodic boundary condition was considered when counting the Ce pairs. In this way, there are in total of 6 Ce^{3+}-Ce^{3+} formed in the lattice shown in the plot.

Supplementary Note 12: APXPS spectra

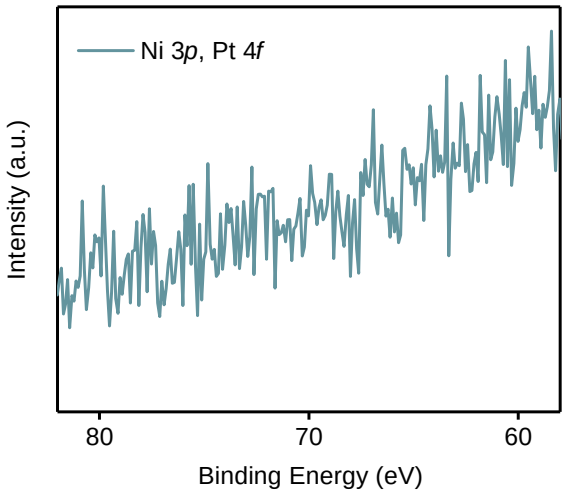

Supplementary Figure 22: Typical Ni 3*p* and Pt 4*f* spectra during experiment. No detectable Ni or Pt peaks are observed. Data collected on $Gd_{0.5}Ce_{0.5}O_{1.75}$ at 450 °C in 0.3 Torr 9:1 CO/CO_2.

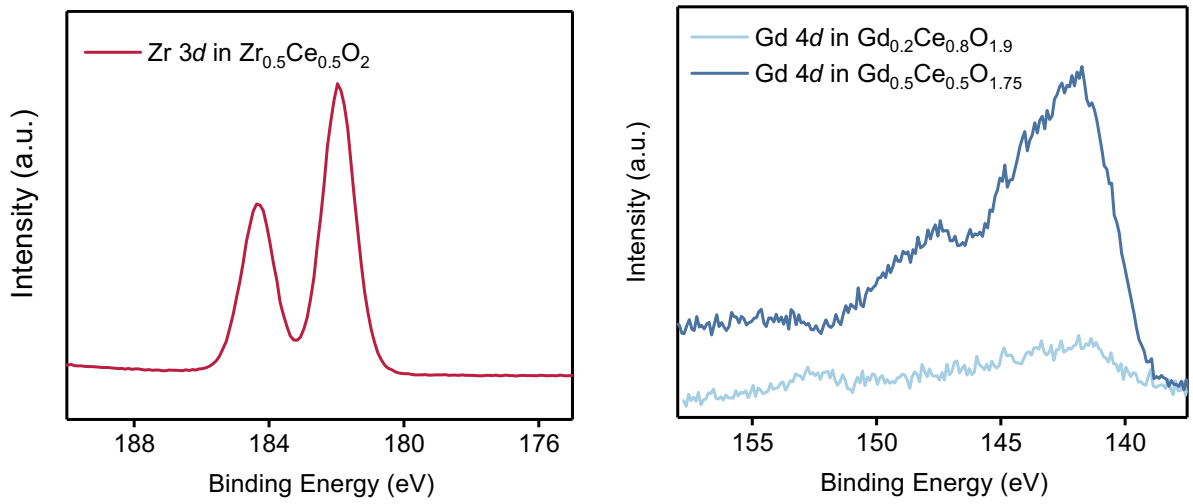

Supplementary Figure 23: Typical Zr $3d$ and Gd $4d$ XPS spectra. Data collected at 450 °C in 0.3 Torr 9:1 CO/CO_2.

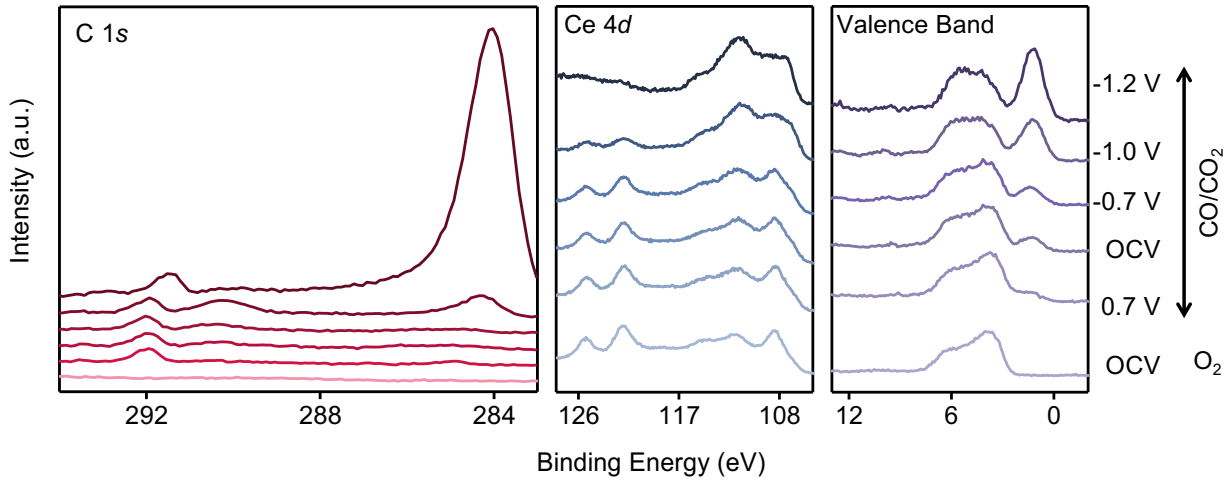

Supplementary Figure 24: XPS spectra of CeO_2. Spectra were collected at 450 °C in 0.3 Torr 9:1 CO/CO_2 and at 350 °C in 20 mTorr O_2, respectively.

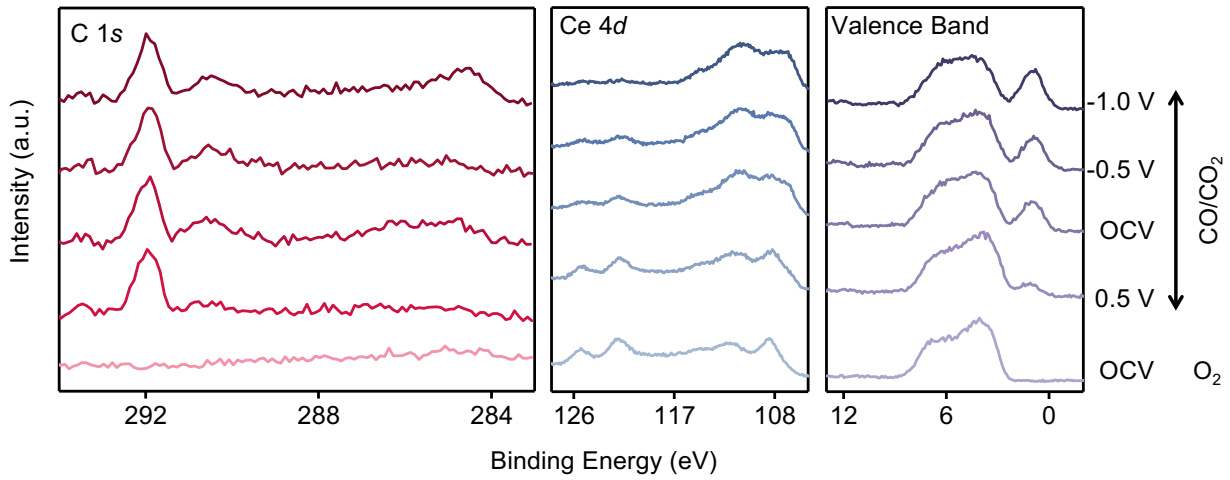

Supplementary Figure 25: XPS spectra of $Zr_{0.5}Ce_{0.5}O_2$. Spectra were collected at 450 °C in 0.3 Torr 9:1 CO/CO_2 and at 350 °C in 20 mTorr O_2, respectively.

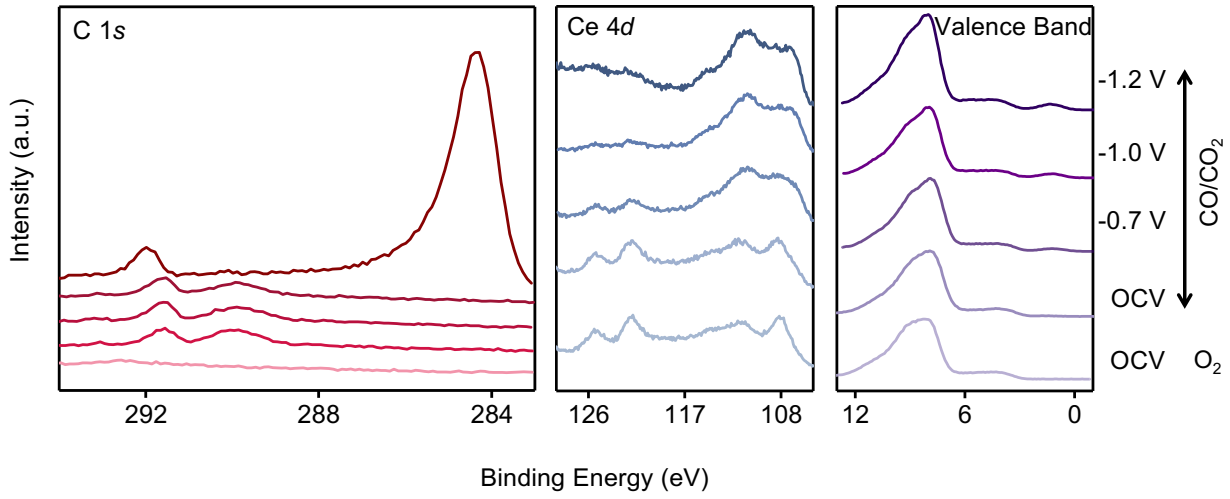

Supplementary Figure 26: XPS spectra of $Gd_{0.5}Ce_{0.5}O_{1.75}$. Spectra were collected at 450 °C in 0.3 Torr 9:1 CO/CO_2 and at 350 °C in 20 mTorr O_2, respectively.

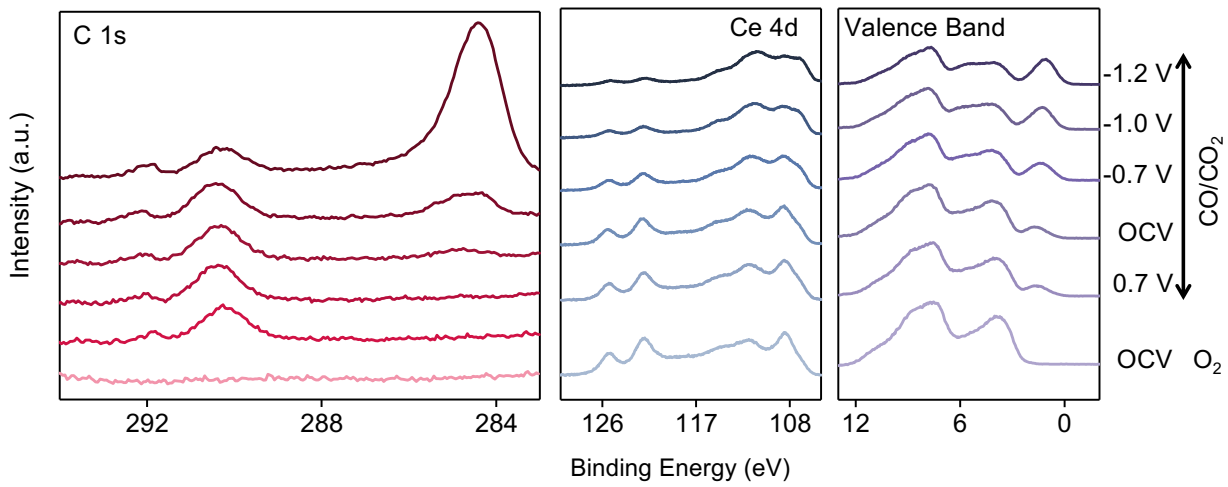

Supplementary Figure 27: XPS spectra of $Gd_{0.2}Ce_{0.8}O_{1.9}$. Spectra were collected at 450 °C in 0.15 Torr 9:1 CO/CO_2 and at 350 °C in 20 mTorr O_2, respectively. Note even at a different total gas pressure, the threshold $[Ce^{3+}]$-carbon relation still exists.

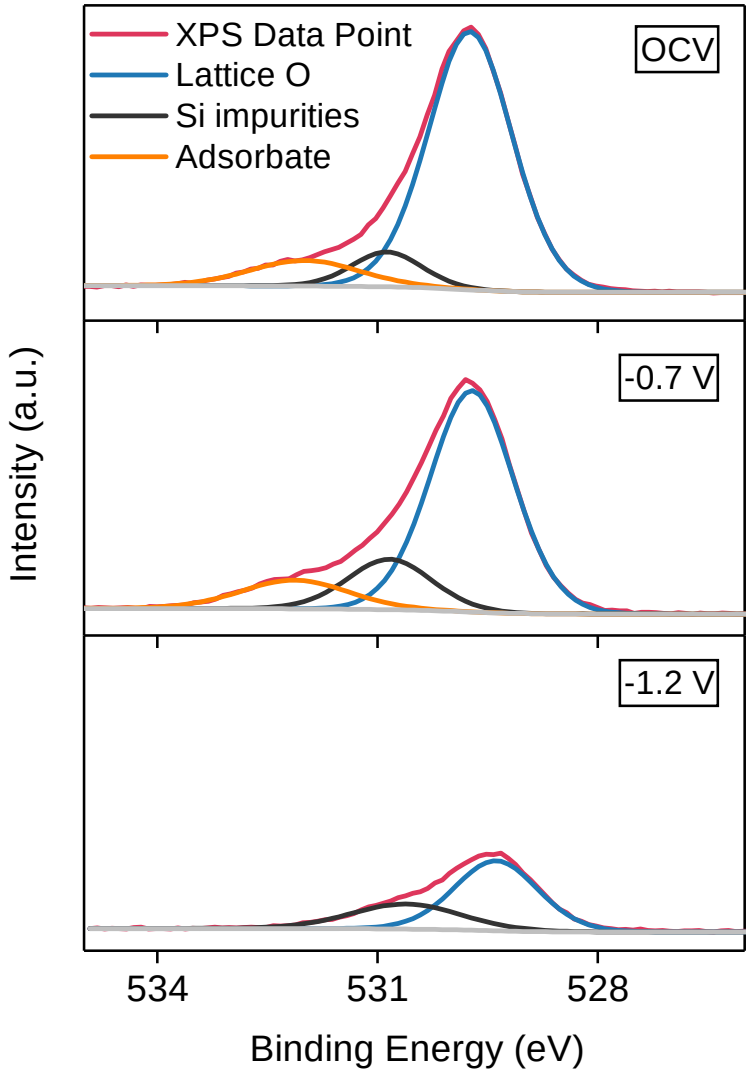

Supplementary Figure 28: Typical O 1*s* spectra during CO_2 electrolysis. Data collected on $Gd_{0.2}Ce_{0.8}O_{1.9}$ at 450 °C in 0.3 Torr 9:1 CO/CO_2 atmosphere at open circuit (OCV), -0.7 V, and -1.2 V electrical bias in sequence.Three dominant features exist: lattice oxygen, Si impurities, and adsorbate, which is in accord with the previous APXPS paper on surface chemistry of CeO_2 during CO_2 electrolysis [15]. After the threshold carbon deposition (-1.2 V), the total intensity of the O 1*s* spectra decreased; and the adsorbate peak vanishes, which is in accord with the C 1*s* spectra behavior shown in Figure 3 in the main text.

References

1. Peng, C. & Zhang, Z. Nitratecitrate combustion synthesis of ce1xgdxo2x/2 powder and its characterization. *Ceram. Int* **33**, 1133 – 1136 (2007).

2. Artini, C. *et al.* Structural features of sm- and gd-doped ceria studied by synchrotron x-ray diffraction and -raman spectroscopy. *Inorg. Chem.* **54**, 4126–4137 (2015).

3. Artini, C., Pani, M., Lausi, A., Masini, R. & Costa, G. A. High temperature structural study of gd-doped ceria by synchrotron x-ray diffraction (673 k t 1073 k). *Inorg. Chem.* **53**, 10140–10149 (2014).

4. Yashima, M., Ohtake, K., Kakihana, M. & Yoshimura, M. Synthesis of metastable tetragonal (t) zirconiaceria solid solutions by the polymerized complex method. *J. Am. Ceram. Soc.* **77**, 2773–2776 (1994).

5. Sharan, R. & Dutta, A. Structural analysis of zr4+ doped ceria, a possible material for ammonia detection in ppm level. *J. Alloys. Compd.* **693**, 936 – 944 (2017).

6. Eren, B., Heine, C., Bluhm, H., Somorjai, G. A. & Salmeron, M. Catalyst chemical state during co oxidation reaction on cu(111) studied with ambient-pressure x-ray photoelectron spectroscopy and near edge x-ray adsorption fine structure spectroscopy. *J. Am. Chem. Soc.* **137**, 11186–11190 (2015).

7. Blomberg, S. *et al.* In situ. *Phys. Rev. Lett.* **110**, 117601 (2013).

8. Favaro, M. *et al.* Subsurface oxide plays a critical role in co2 activation by cu(111) surfaces to form chemisorbed co2, the first step in reduction of co2. *Proc. Natl. Acad. Sci. U.S.A.* **114**, 6706–6711 (2017).

9. Mullins, D., Overbury, S. & Huntley, D. Electron spectroscopy of single crystal and polycrystalline cerium oxide surfaces. *Surf. Sci.* **409**, 307 – 319 (1998).

10. Knoll, G. F. *Radiation detection and measurement* (John Wiley & Sons, 2010).

11. Strydom, C. & Strydom, H. X-ray photoelectron spectroscopy determination of the ce(iii)/ce(iv) ratio in cerium compounds. *Inorganica Chim. Acta* **161**, 7 – 9 (1989).

12. Xiao, W., Guo, Q. & Wang, E. Transformation of ceo2(1 1 1) to ce2o3(0 0 0 1) films. *Chem. Phys. Lett.* **368**, 527 – 531 (2003).

13. Feng, Z. A., El Gabaly, F., Ye, X., Shen, Z.-X. & Chueh, W. C. Fast vacancy-mediated oxygen ion incorporation across the ceria–gas electrochemical interface. *Nat. Commun.* **5** (2014).

14. Chueh, W. C. *et al.* Highly enhanced concentration and stability of reactive ce3+ on doped ceo2 surface revealed in operando. *Chem. Mater.* **24**, 1876–1882 (2012).

15. Feng, Z. A., Machala, M. L. & Chueh, W. C. Surface electrochemistry of co2 reduction and co oxidation on sm-doped ceo2-x: coupling between ce3+ and carbonate adsorbates. *Phys. Chem. Chem. Phys.* **17**, 12273–12281 (2015).

16. Hofmann, S. *Auger-and X-ray photoelectron spectroscopy in materials science: a user-oriented guide*, vol. 49 (2013).

17. Yeh, J. & Lindau, I. Atomic subshell photoionization cross sections and asymmetry parameters: 1 z 103. *Atomic Data and Nuclear Data Tables* **32**, 1 – 155 (1985).

18. Murday, J. S., Dunlap, B. I., Hutson, F. L. & Oelhafen, P. Carbon KVV auger line shapes of graphite and stage-one cesium and lithium intercalated graphite. *Phys. Rev. B* **24**, 4764–4770 (1981).

19. Gunter, P. L. J., Jong, A. M. D., Niemantsverdriet, J. W. & Rheiter, H. J. H. Evaluation of takeoffangledependent xps for determining the thickness of passivation layers on aluminium and silicon. *Surface and Interface Analysis* **19**, 161–164 (1992).

20. Tanuma, S., Powell, C. & Penn, D. Calculations of electron inelastic mean free paths. ix. data for 41 elemental solids over the 50 ev to 30 kev range. *Surf. Interface Anal.* **43**, 689–713 (2011).

21. Li, X., Cai, W., Colombo, L. & Ruoff, R. S. Evolution of graphene growth on ni and cu by carbon isotope labeling. *Nano Letters* **9**, 4268–4272 (2009).

22. Nenning, A. *et al.* Ambient pressure xps study of mixed conducting perovskite-type sofc cathode and anode materials under well-defined electrochemical polarization. *J. Phys. Chem. C* **120**, 1461–1471 (2016).

23. Lu, Q. & Yildiz, B. Voltage-controlled topotactic phase transition in thin-film srcoox monitored by in situ x-ray diffraction. *Nano Lett.* **16**, 1186–1193 (2016).

24. El Gabaly, F. *et al.* Measuring individual overpotentials in an operating solid-oxide electrochemical cell. *Phys. Chem. Chem. Phys.* **12**, 12138–12145 (2010).

25. Eufinger, J.-P. *et al.* The model case of an oxygen storage catalyst - non-stoichiometry, point defects and electrical conductivity of single crystalline ceo2-zro2-y2o3 solid solutions. *Phys. Chem. Chem. Phys.* **16**, 25583–25600 (2014).

26. Ramírez-Cabrera, E., Atkinson, A. & Chadwick, D. The influence of point defects on the resistance of ceria to carbon deposition in hydrocarbon catalysis. *Solid State Ionics* **136-137**, 825 – 831 (2000).

27. Lykhach, Y. *et al.* Counting electrons on supported nanoparticles. *Nat. Mater.* **15**, 284–288 (2016).